# Light Transmission Through Space-Time-Modulated Josephson Junction Arrays and Application to Quantum Angular-Frequency Beam Multiplexing

Sajjad Taravati, *Senior Member, IEEE*

***Abstract*—Josephson junctions, as pivotal components of modern technologies such as superconducting quantum computing, owe their prominence to their unique nonlinear properties at low temperatures. Despite their extensive use in static configurations, the study of dynamic Josephson junctions, under space-time (ST) modulation, remains largely unexplored. This study investigates the interaction and transmission of light through arrays of space-time-modulated (STM) Josephson junctions. A comprehensive mathematical framework is presented to model the propagation of electric and magnetic fields within and beyond these structures. We demonstrate how such dynamic arrays enable unique four-dimensional light manipulation, leading to angular-frequency beam multiplexing through a seamless integration of frequency conversion and beam-splitting functionalities. These advancements open new horizons for electromagnetic field engineering, with far-reaching implications for superconducting quantum technologies, next-generation wireless communications, biomedical sensing, and radar systems.**

***Index Terms*—Josephson junctions, superconducting time modulation, quantum technologies, Maxwell's equations, beam multiplexing.**

## I. Introduction

Josephson junctions, comprising an insulator between two superconducting layers, are essential in superconducting electronics [1], [2]. These nonlinear devices enable supercurrent via Cooper pair tunneling, allowing resistance-free current flow. Their quantum-level electromagnetic wave manipulation has enabled applications from classical electronics to quantum technologies. In quantum computing, they form qubits for high-coherence state manipulation and are used in parametric amplifiers, quantum-limited detectors, and frequency converters. They also underpin precision metrology, enabling voltage standards and accurate microwave generation. Beyond this, they are explored for quantum sensors in astrophysics, quantum communication systems, and scalable superconducting circuits. Despite their established applications, Josephson junctions in space-time-modulated (STM) systems remain largely unexplored [3]–[5]. Our work pioneers the study of electromagnetic wave interactions with STM Josephson junction arrays, enabling nonreciprocal light propagation, tunable frequency conversion, and tailored photon interactions. These advances hold transformative potential for quantum communication, photon-based information processing, and other quantum technologies.

S. Taravati is with the Faculty of Engineering and Physical Sciences, University of Southampton, Southampton SO17 1BJ, UK (e-mail: s.taravati@soton.ac.uk).

Manuscript received ***, 2025; revised ***, 2025.

Linear STM structures have gained attention for applications in wireless communication, photonics, and radar technologies [6]–[19]. These systems modulate electrical permittivity in space and time [20]–[25], enabling linear STM metasurfaces at microwave [26]–[28] and optical frequencies [29]–[31]. They support functionalities like nonreciprocal transmission [14], [32], target recognition [33], isolators [34]–[36], temporal aiming [37], frequency conversion [38], [39], circulators [40], [41], nonreciprocal antennas [42], parametric amplification [43], [44], and multifunctional operations [45], [46]. However, conventional time-modulated devices, relying on varactors, transistors, and diodes, are unsuitable for millikelvin environments due to noise and operational constraints. In contrast, STM Josephson junction arrays excel in such conditions, leveraging strong harmonic coupling for efficient frequency conversion, even at high modulation-to-signal ratios. Their compactness, efficiency, and precision make them ideal for superconducting quantum technologies, overcoming limitations of linear STM systems like phase matching and dispersion.

This paper demonstrates angular-frequency beam multiplexing using an array of dynamic Josephson junctions, enabling frequency conversion and beam-splitting—key functionalities for quantum technologies and wireless communications. In quantum computing, frequency converters mediate interactions between qubits at different frequencies, reducing crosstalk and enhancing fidelity, which is critical for quantum error correction [47], [48]. They also enable quantum state transduction between microwave and optical photons, essential for long-distance quantum communication and hybrid quantum systems [49]. In quantum sensing, ultra-low-noise frequency converters at millikelvin temperatures enhance sensitivity for applications like dark matter detection and gravitational wave sensing [50], [51]. In wireless communications, frequency conversion bridges different frequency bands, optimizing bandwidth in multiband networks like 5G, while beam-splitting enhances spectral efficiency and reliability in massive MIMO systems [52]. These operations are also critical for satellite and airborne communication systems, ensuring stable, high-speed links. While the proposed Josephson array and mathematical model encompass general light interaction with STM systems, this work focuses on angular-frequency beam multiplexing. The cryogenic-compatible array is applicable to wireless communications and holds significant potential for superconducting quantum computing, where photon interactions with Josephson junctions are pivotal.

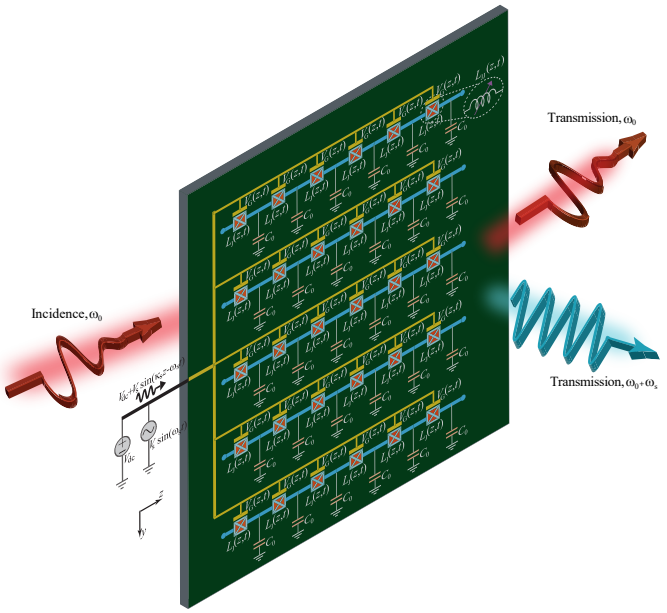


Fig. 1. Light interaction with an array of STM Josephson junctions leading to angular-frequency beam multiplexing.

This paper is organized as follows. Section II presents the theoretical framework and mathematical modeling of light interaction with STM Josephson junction arrays. Section II-C analyzes light incidence and transmission through these arrays, detailing the underlying mechanisms. Section III proposes a practical implementation of the array and demonstrates its frequency-angular beam multiplexing capabilities through full-wave numerical simulations and conversion efficiency analysis. Finally, Section V summarizes the findings and concludes the paper.

## II. Theoretical Implications

### A. Array of STM Josephson junctions

The structure under study, shown in Fig. 1, consists of an array of STM Josephson junctions. A space-time (ST)-varying voltage is passing through the array and modulating the array inclusions. The voltage is given by $V(z,t) = V_{\rm dc} + V_{\rm rf}\sin[\kappa_{\rm s}z - \omega_{\rm s}t + \phi]$. Here, $V_{\rm dc}$ is the dc voltage component, representing a constant bias applied to the system, $V_{\rm rf}$ is the amplitude of the rf (radio frequency) voltage component, representing the time-varying modulation, $\kappa_{\rm s}$ is the spatial wavenumber of the modulation, describing the spatial periodicity of the applied voltage, $\omega_{\rm s}$ is the angular frequency of the modulation, describing the temporal periodicity of the applied voltage, and $\phi$ is the phase offset of the modulation, accounting for any initial phase difference in the applied signal. The phase velocity of the ST modulation reads

$$\gamma = \frac{v_{\rm s}}{v_{\rm b}} = \frac{\omega_{\rm s}}{v_{\rm b}\kappa_{\rm s}}, \tag{1}$$

which may either exceed or fall below the phase velocity of the background medium, denoted as $v_{\rm b} = c/\sqrt{\mu_{\rm r}\epsilon_{\rm r}}$, where $c = 1/\sqrt{\mu_0\epsilon_0}$ is the speed of light in vacuum, and $\epsilon_{\rm r}$ and $\mu_{\rm r}$ representing, respectively, the relative electric permittivity and relative magnetic permeability of the background medium. The space-time velocity ratio. Eq. (1) characterizes the relationship between the modulation and background phase velocities. In the limiting cases, $\gamma = 0$ corresponds to a purely space-modulated medium, while $\gamma \to \infty$ describes a purely time-modulated medium [53].

The current density of the *superconducting* array reads

$$J_{\rm s}(z,t) = I_0\sin[\rho(z,t)], \tag{2a}$$

where $I_0$ is the critical current and

$$\begin{aligned}\rho(z,t) &= 2\pi\frac{\Phi(z,t)}{\Phi_0} = \frac{2\pi}{\Phi_0}\int_{-\infty}^{t} V(z,t')dt' \\ &= \frac{2\pi}{\Phi_0}\left(tV_{\rm dc} + \frac{1}{\omega_{\rm s}}V_{\rm rf}\sin[\kappa_{\rm s}z - \omega_{\rm s}t + \phi]\right),\end{aligned} \tag{2b}$$

where $\Phi_0$ is the magnetic flux quantum and $\Phi(z,t)$ is the ST-dependent magnetic flux. The time derivative of the current density, which is directly related to the voltage $V(z,t)$, is given by

$$\frac{dJ(z,t)}{dt} = \frac{2\pi I_0\cos[\rho(z,t)]}{\Phi_0}V(z,t), \tag{2c}$$

which gives $V(z,t) = L_{\rm s}(z,t)dJ(z,t)/dt$. Consequently, the effective STM magnetic permeability of the array is expressed as

$$\mu_{\rm s}(z,t) = \frac{lL_{\rm s}(z,t)}{\mu_0 A} = \frac{1}{G_\mu\cos\left(\widetilde{\Phi}_{\rm dc} + \widetilde{\Phi}_{\rm rf}\sin[\kappa_{\rm s}z - \omega_{\rm s}t + \phi]\right)}, \tag{3}$$

where $G_\mu = 2\pi\mu_0 I_0 A/(\Phi_0 l)$, where $l$ and $A$ are the length and area of the STM array, respectively. Here, $\widetilde{\Phi}_{\rm dc} = 2\pi\Phi_{\rm dc}/\Phi_0$ and $\widetilde{\Phi}_{\rm rf} = 2\pi\Phi_{\rm rf}/\Phi_0$ are the dc and rf fluxes, respectively, representing the static and dynamic modulation amplitudes. Since the array is periodic in both space and time, the magnetic permeability of the array may be decomposed into ST Floquet-Bloch harmonics, as

$$g(z,t) = \frac{1}{\mu_{\rm s}(z,t)} = \sum_{m=-\infty}^{+\infty} g_m e^{-jm(\kappa_{\rm s}z - \omega_{\rm s}t + \phi)}, \tag{4a}$$

To find the unknown coefficients $g_m$s we first define $\psi = \kappa_{\rm s}z - \omega_{\rm s}t + \phi$, and then expand the cosine term in Eq. (3), as

$$\begin{aligned}\cos\left(\widetilde{\Phi}_{\rm dc} + \widetilde{\Phi}_{\rm rf}\sin\psi\right) &= \cos\left(\widetilde{\Phi}_{\rm dc}\right)\cos\left(\widetilde{\Phi}_{\rm rf}\sin\psi\right) \\ &\quad - \sin\left(\widetilde{\Phi}_{\rm dc}\right)\sin\left(\widetilde{\Phi}_{\rm rf}\sin\psi\right).\end{aligned} \tag{4b}$$

where the cosine and sine terms can be further expanded using the Taylor's series expansion. Therefore, the $g_m$s in Eq. (4a) read

$$g_0 = G_\mu\left(1 - \frac{\widetilde{\Phi}_{\rm rf}^2}{4} + \frac{\widetilde{\Phi}_{\rm rf}^4}{64} - \frac{\widetilde{\Phi}_{\rm rf}^6}{2304} + \frac{\widetilde{\Phi}_{\rm rf}^8}{147456}\right)\cos\widetilde{\Phi}_{\rm dc}, \tag{4c}$$

$$g_1 = -g_{-1} = \frac{G_\mu}{2j}\left(\widetilde{\Phi}_{\rm rf} - \frac{\widetilde{\Phi}_{\rm rf}^3}{8} + \frac{\widetilde{\Phi}_{\rm rf}^5}{192} - \frac{\widetilde{\Phi}_{\rm rf}^7}{9216}\right)\sin\widetilde{\Phi}_{\rm dc}, \tag{4d}$$

$$g_2 = g_{-2} = \frac{G_\mu}{8}\left(\widetilde{\Phi}_{\rm rf}^2 - \frac{\widetilde{\Phi}_{\rm rf}^4}{12} + \frac{\widetilde{\Phi}_{\rm rf}^6}{384} - \frac{\widetilde{\Phi}_{\rm rf}^8}{23040}\right)\cos\widetilde{\Phi}_{\rm dc}, \tag{4e}$$

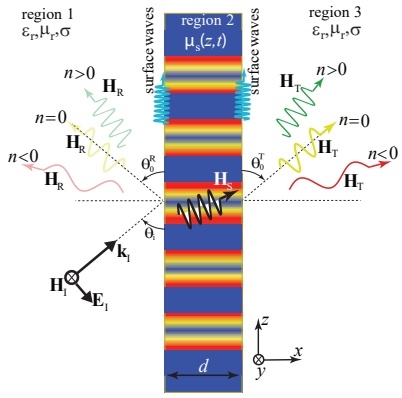


Fig. 2. Wave scattering from a STM superconducting surface.

$$g_3 = -g_{-3} = \frac{G_\mu}{j48}\left(\widetilde{\Phi}_{\rm rf}^3 - \frac{\widetilde{\Phi}_{\rm rf}^5}{16} + \frac{\widetilde{\Phi}_{\rm rf}^7}{640}\right)\sin\widetilde{\Phi}_{\rm dc}, \tag{4f}$$

$$g_4 = g_{-4} = \frac{G_\mu}{384}\left(\widetilde{\Phi}_{\rm rf}^4 - \frac{\widetilde{\Phi}_{\rm rf}^6}{20} + \frac{\widetilde{\Phi}_{\rm rf}^8}{960}\right)\cos\widetilde{\Phi}_{\rm dc}, \tag{4g}$$

$$g_5 = -g_{-5} = \frac{G_\mu}{j3840}\left(\widetilde{\Phi}_{\rm rf}^5 - \frac{\widetilde{\Phi}_{\rm rf}^7}{24}\right)\sin\widetilde{\Phi}_{\rm dc}, \tag{4h}$$

$$g_6 = g_{-6} = \frac{G_\mu}{46080}\left(\widetilde{\Phi}_{\rm rf}^6 - \frac{\widetilde{\Phi}_{\rm rf}^8}{28}\right)\cos\widetilde{\Phi}_{\rm dc}, \tag{4i}$$

$$g_7 = -g_{-7} = \frac{G_\mu}{j645120}\widetilde{\Phi}_{\rm rf}^7\sin\widetilde{\Phi}_{\rm dc}, \tag{4j}$$

$$g_8 = g_{-8} = \frac{G_\mu}{10321920}\widetilde{\Phi}_{\rm rf}^8\cos\widetilde{\Phi}_{\rm dc}. \tag{4k}$$

### *B. Floquet-Bloch ST Harmonics*

Figure 2 illustrates the transmission and reflection of light from an array of STM Josephson junctions, characterized by the STM permeability described in Eq. (3). Taking into account the ST periodicity of the STM array, the electric and magnetic fields within the slab can be decomposed into a series of Floquet-Bloch harmonics, capturing the contributions of both spatial and temporal modulations. This expansion provides a comprehensive framework to describe wave interactions in periodic structures. Consequently, the transverse magnetic (TM) wave propagation within the slab can be expressed in terms of these harmonics, where each harmonic corresponds to a distinct combination of spatial and temporal frequencies. Consequently, the TM wave propagation within the slab can be expressed as

$$\mathbf{H}_{\rm s}(x,z,t) = \hat{\mathbf{y}}\sum_n H_n e^{-j[k_x x+\kappa_n z-\omega_n t]}, \tag{5a}$$

$$\begin{aligned}\mathbf{E}_{\rm s}(x,z,t) &= -\eta_2\left[\hat{\mathbf{k}}_{\rm s}\times\mathbf{H}_{\rm s}(x,z,t)\right]\\ &= \eta_2\sum_n\left(\hat{\mathbf{x}}\sin(\theta_n) - \hat{\mathbf{z}}\cos(\theta_{\rm i})\right)H_n e^{-j\left[k_x x+\kappa_n z-\omega_n t\right]},\end{aligned} \tag{5b}$$

where $\eta_2$ is the characteristic impedance of the background medium of the array, and $\hat{\mathbf{k}}_{\rm s} = \hat{\mathbf{x}}\cos(\theta_{\rm i}) + \hat{\mathbf{z}}\kappa_n/k_n$ is the wavevector of the light in the array. Here, $\theta_{\rm i}$ is the angle of incidence between the incident wave and the array boundary, $\kappa_n = \kappa_0 + n\kappa_{\rm s}$ is the $z$-component of the wavenumber for the $n$th ST harmonic inside the array, and $k_n = k_0 + n\omega_{\rm s}/v_{\rm b}$ is the total wavenumber of the $n$th harmonic. In these expressions, $k_0 = \omega_0/c$ is the wavenumber of the incident light, $\omega_0$ is the angular frequency of the incident light, and $\omega_{\rm s}$ is the angular frequency of the ST modulation. In addition, the $x$-component of the wavenumber is given by $k_x = k_0\cos(\theta_{\rm i})$, and the angle $\theta_n$ for the $n$th ST harmonic satisfies $\sin(\theta_n) = \kappa_n/k_n$. The source-free wave equation for the system is

$$\nabla^2\mathbf{H}_{\rm s}(x,z,t) - \frac{1}{c^2}\frac{\partial^2\left[\mu_{\rm s}(z,t)\mathbf{H}_{\rm s}(x,z,t)\right]}{\partial t^2} = 0. \tag{6a}$$

Substituting the magnetic field expression from Eq. (5a) into the wave equation (6a) yields

$$\begin{aligned}&\sum_n (k_x^2+\kappa_n^2)H_n e^{-j[k_x x+\kappa_n z-\omega_n t]}\\ &-\frac{1}{c^2}\frac{\partial^2}{\partial t^2}\sum_{m,n}\tilde{\mu}_m H_{m+n}e^{-j[k_x x+\kappa_n z-\omega_n t+\phi]} = 0,\end{aligned} \tag{6b}$$

which may be cast as

$$H_n e^{j\phi}\left[\frac{k_x^2+\kappa_n^2}{k_n^2}\right] - \sum_m \tilde{\mu}_m H_{m+n} = 0, \tag{6c}$$

where $\tilde{\mu}_m = 1/g_m$. Truncating to $2N+1$ terms yields

$$[\mathbf{U}]\cdot[\overrightarrow{H}] = 0. \tag{7a}$$

The matrix $[\mathbf{U}]$ is a square matrix of size $(2N+1)\times(2N+1)$, with elements defined as

$$\begin{aligned}U_{nn} &= \frac{k_x^2+\kappa_n^2}{k_n^2} - \tilde{\mu}_0,\\ U_{nm} &= -\tilde{\mu}_{m+n}, \quad \text{for } n\neq m,\end{aligned} \tag{7b}$$

where

$$[\mathbf{U}] = \begin{bmatrix} c_{-N} & \tilde{\mu}_1 & \tilde{\mu}_2 & \cdots & \tilde{\mu}_{M-2} & \tilde{\mu}_{M-1} & \tilde{\mu}_M \\ \tilde{\mu}_{-1} & c_{-N+1} & \tilde{\mu}_1 & \cdots & \tilde{\mu}_{M-3} & \tilde{\mu}_{M-2} & \tilde{\mu}_{M-1} \\ \vdots & \vdots & \vdots & \ddots & \vdots & \vdots & \vdots \\ \tilde{\mu}_{-M+1} & \tilde{\mu}_{-M+2} & \tilde{\mu}_{-M+3} & \cdots & \tilde{\mu}_{-1} & c_{N-1} & \tilde{\mu}_1 \\ \tilde{\mu}_{-M} & \tilde{\mu}_{-M+1} & \tilde{\mu}_{-M+2} & \cdots & \tilde{\mu}_{-2} & \tilde{\mu}_{-1} & c_N \end{bmatrix}, \tag{7c}$$

where $c_n = \tilde{\mu}_0 - (k_x^2+\kappa_n^2)/k_n^2$. The vector of unknowns $[\overrightarrow{H}]$ in Eq. (7a) is a $(2N+1)\times 1$ vector containing the $H_n$ values. For non-trivial solutions (i.e., $[\overrightarrow{H}] \neq 0$), the matrix $[\mathbf{U}]$ must be singular, meaning its determinant is zero, that is,

$$\det[\mathbf{U}] = 0. \tag{7d}$$

The condition outlined in Eq. (7d) determines when the system permits wave propagation, offering the dispersion relationship typically expressed as $\omega(k)$ or $k(\omega)$. The matrix $[\mathbf{U}]$ encapsulates material properties, such as permittivity, permeability, and conductivity, which collectively influence wave behavior. Its components depend on the wavevector ($\kappa_n$) and frequency ($\omega_n$), creating a direct relationship between the two. By enforcing $\det[\mathbf{U}] = 0$, the propagation criteria

are established, revealing how frequency and wavevector are interconnected. This relationship, expressed as $\omega_n(\kappa_n)$ or $\kappa_n(\omega_n)$, provides insight into the system's allowed frequencies, wavevectors, group velocity, phase velocity, and band structure. Thus, Eq. (7d) serves as a critical criterion for wave propagation, and solving it yields the dispersion relation that defines wave dynamics within the medium.

The matrix $[\mathbf{U}]$, along with the truncated set of $g_n$ coefficients, illustrates the effects of nonlinearity. In nonlinear systems, energy from the primary harmonic modes ($U_{nn}$) is redistributed across an infinite series of other harmonic modes ($U_{nm}$, where $n \neq m$, $-\infty < n, m < +\infty$). This contrasts with linear STM media [8], where energy is redistributed among *all*, in contrast to linear STM arrays where energy is redistributed only among the nearest neighboring harmonic modes harmonic modes ($U_{n,n-1}$ and $U_{n,n+1}$). Nonlinear interactions enable energy transfer across a wider range of harmonic frequencies, allowing the incident wave to excite higher-order harmonics efficiently. This is due to the ability of nonlinear systems to sustain the high-frequency modulation necessary for such energy redistribution.

### C. Wave Incidence and Transmission

The TM incident magnetic and electric fields read

$$\mathbf{H}_{\mathrm{I}}(x,z,t) = \hat{\mathbf{y}} h_0 e^{(j\omega_0 t)} \cdot e^{-j[k_x x + k_0 \sin(\theta_{\mathrm{i}}) z]} \tag{8a}$$

$$\begin{aligned}\mathbf{E}_{\mathrm{I}}(x,z,t) &= -\eta_1 \left[\hat{\mathbf{k}}_{\mathrm{I}} \times \mathbf{H}_{\mathrm{I}}(x,z,t)\right] \\ &= \eta_1 \left[\hat{\mathbf{x}} \sin(\theta_{\mathrm{i}}) - \hat{\mathbf{z}} \cos(\theta_{\mathrm{i}})\right] \cdot h_0 e^{j\omega_0 t} \cdot e^{-j[k_x x + k_0 \sin(\theta_{\mathrm{i}}) z]}\end{aligned} \tag{8b}$$

where $\eta_1 = \sqrt{\mu_0 \mu_1 / (\epsilon_0 \epsilon_1)}$. The reflected and transmitted electric fields outside of the slab may be defined as

$$\mathbf{H}_{\mathrm{R}}(x,z,t) = \hat{\mathbf{y}} \sum_{n=-\infty}^{\infty} R_n e^{-j\left[k_x x - k_{0n} \sin(\theta_n^{\mathrm{R}}) z - \omega_n t\right]}, \tag{9a}$$

$$\begin{aligned}\mathbf{E}_{\mathrm{R}}(x,z,t) &= -\eta_1 [\hat{\mathbf{k}}_{\mathrm{R}} \times \mathbf{H}_{\mathrm{R}}(x,z,t)] \\ &= -\eta_1 \left[\hat{\mathbf{x}} \sin(\theta_n^{\mathrm{R}}) + \hat{\mathbf{z}} \cos(\theta_{\mathrm{i}})\right] \cdot R_n e^{-j\left[k_x x - k_{0n} \sin(\theta_n^{\mathrm{R}}) z - \omega_n t\right]},\end{aligned} \tag{9b}$$

$$\mathbf{H}_{\mathrm{T}}(x,z,t) = \hat{\mathbf{y}} \sum_{n} T_n e^{-j\left[k_x x + k_{0n} \sin(\theta_n^{\mathrm{T}}) z - \omega_n t\right]}, \tag{9c}$$

$$\begin{aligned}\mathbf{E}_{\mathrm{T}}(x,z,t) &= -\eta_3 [\hat{\mathbf{k}}_{\mathrm{T}} \times \mathbf{H}_{\mathrm{T}}(x,z,t)] \\ &= \eta_3 \sum_{n} \left[\hat{\mathbf{x}} \sin(\theta_n^{\mathrm{T}}) - \hat{\mathbf{z}} \cos(\theta_{\mathrm{i}})\right] \cdot T_n e^{-j\left[k_x x + k_{0n} \sin(\theta_n^{\mathrm{T}}) z - \omega_n t\right]},\end{aligned} \tag{9d}$$

where $\eta_3 = \sqrt{\mu_0 \mu_3 / (\epsilon_0 \epsilon_3)}$. continuity of the tangential components of the electromagnetic fields at $z = 0$ and $z = d$ to find the unknown field amplitudes $H_0$, $R_n$ and $T_n$. The electric and magnetic fields continuity conditions between regions 1 and 2 at $z = 0$, $H_{1y}(x,0,t) = H_{2y}(x,0,t)$ and $E_{1x}(x,0,t) = E_{2x}(x,0,t)$ read

$$\delta_{n0} h_0 + R_n = H_n, \tag{10a}$$

$$\eta_1 \sin(\theta_{\mathrm{i}}) \delta_{n0} h_0 - \eta_1 \sin(\theta_n^{\mathrm{R}}) R_n = \eta_2 \sin(\theta_n) H_n. \tag{10b}$$

By solving the above two equations simultaneously, we achieve

$$H_0 = \frac{2\eta_1 h_0 \sin(\theta_{\mathrm{i}})}{\eta_1 \sin(\theta_{\mathrm{i}}) + \eta_2 \sin(\theta_0)}, \tag{10c}$$

$$R_n = H_n - \delta_{n0} h_0. \tag{10d}$$

The continuity condition of electric and magnetic fields between regions 2 and 3 at $z = d$, $H_{2y}(x,d,t) = H_{3y}(x,d,t)$ and $E_{2x}(x,d,t) = E_{3x}(x,d,t)$, reduces to

$$H_n e^{-j\kappa_n d} = T_n e^{-jk_{0n} \sin(\theta_n^{\mathrm{T}}) d}, \tag{11a}$$

$$\eta_2 \sin(\theta_n) H_n e^{-j\kappa_n d} = \eta_3 \sin(\theta_n^{\mathrm{T}}) T_n e^{-jk_n \sin(\theta_n^{\mathrm{T}}) d}, \tag{11b}$$

which gives

$$T_n = \frac{\eta_2 \sin(\theta_n)}{\eta_3 \sin(\theta_n^{\mathrm{T}})} H_n e^{-j[\kappa_n - k_n \sin(\theta_n^{\mathrm{T}})] d}. \tag{11c}$$

The scattering angles of the transmitted ST harmonics, denoted as $\theta_n^{\mathrm{T}}$, can be derived from the Helmholtz relations. These relations ensure that the wavevector components satisfy the dispersion constraints within the STM medium. Mathematically, this is expressed as $[k_0 \cos(\theta_{\mathrm{i}})]^2 + [\kappa_n \sin(\theta_n)]^2 = k_n^2$.

## III. Frequency-Angular Beam Multiplexing

Figure 3 illustrates the experimental prototype design of a STM Josephson junction array. Each Josephson junction is formed by a thin dielectric tunnel barrier sandwiched between two superconducting layers. The superconducting layers are fabricated using materials such as aluminum (Al) or niobium (Nb), chosen for their high critical current densities, low microwave losses, and compatibility with cryogenic environments essential for quantum applications. The Josephson junctions are patterned on a high-quality substrate, commonly silicon (Si) or sapphire ($Al_2O_3$), both known for their excellent thermal conductivity and low dielectric loss at cryogenic temperatures. The substrate provides mechanical stability and reduces parasitic effects like crosstalk and substrate-induced losses, essential for high-frequency, high-fidelity operation. For ST modulation, a modulation signal is applied to the Josephson junctions via a power divider on the right, ensuring uniform signal distribution across the array for precise control over ST-dependent electromagnetic properties. High-quality coaxial cables or superconducting transmission lines deliver the signal with minimal attenuation and phase noise. On the left, another power divider directs the signal to a matched load to prevent reflections. The entire setup operates in a cryogenic environment, typically a dilution refrigerator, to maintain superconductivity and suppress thermal noise, with electromagnetic shielding added to minimize external interference and ensure stable ST modulation.

According to the dispersion relation in Eq. (7d), a three-dimensional dispersion diagram can be constructed to visualize the wave dynamics in the STM array. Figure 4(a) qualitatively depicts this three-dimensional dispersion diagram, illustrating the interdependence of the frequency ($\omega_n$), the $z$-component of the wavevector ($\kappa_n$), the $x$-component of the wavevector ($k_x$), and the modulation frequency ($\omega_{\mathrm{s}}$). The $x$-component of

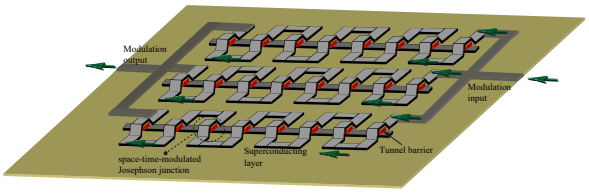


Fig. 3. Experimental prototype design of a STM Josephson junction array.

the wavevector, $k_x$, is particularly significant as it represents the angle of incidence ($\theta_{\rm i} = \cos^{-1}(k_x/k_0)$). The dispersion diagram features a series of double semi-cones aligned along the $\omega_n$ axis, each corresponding to a specific ST harmonic. The positive-slope regions of the semi-cones, with respect to the $(\omega_n, \kappa_n)$ plane, represent a positive group delay corresponding to forward-propagating waves, while the negative-slope regions indicate negative group delay corresponding to backward-propagating waves. The steepness of the semi-cones is determined by the ST modulation parameter, $\widetilde{\Phi}_{\rm dc}$, such that increasing $\widetilde{\Phi}_{\rm dc}$ results in a greater slope, reflecting enhanced modulation strength. At the center of each double semi-cone lies an electromagnetic bandgap, which is influenced by $\widetilde{\Phi}_{\rm dc}$.As $\widetilde{\Phi}_{\rm dc}$ increases, the bandgap widens, signifying enhanced coupling between harmonics and more efficient energy redistribution across them. The slope of the higher-order ST harmonic cones is directly proportional to the ST modulation amplitude $\widetilde{\Phi}_{\rm rf}$. When $\widetilde{\Phi}_{\rm rf} \to 0$, the higher-order harmonic cones vanish entirely, reflecting the absence of dynamic modulation and reducing the system to a purely static problem. This intricate interplay between the modulation parameters, $\widetilde{\Phi}_{\rm dc}$ and $\widetilde{\Phi}_{\rm rf}$, highlights the tunability of the system's dispersion characteristics and provides valuable insights into the propagation and manipulation of waves in STM Josephson junctions.

Figures 4(b) through 4(g) present the analytical two-dimensional dispersion diagrams ($\omega_n$ versus $\kappa_n$) for various operational regimes of the STM Josephson junction array, calculated using Eq. (7d). These diagrams illustrate the influence of the ST modulation parameters, $\widetilde{\Phi}_{\rm dc}$ and $\widetilde{\Phi}_{\rm rf}$, on the system's dispersion characteristics. Figure 4(b) shows the case where $\widetilde{\Phi}_{\rm dc} \to 0$ and $\widetilde{\Phi}_{\rm rf} \to 0$, resulting in a conventional dispersion diagram without bandgaps or harmonic coupling. Figure 4(c) depicts $\widetilde{\Phi}_{\rm dc} = 0.7$ and $\widetilde{\Phi}_{\rm rf} \to 0$, where static modulation tilts the $n = 0$ dispersion curve and introduces a bandgap at the center of the $n = 0$ double semi-cone. Figure 4(d) demonstrates weak dynamic modulation ($\widetilde{\Phi}_{\rm rf} = 0.1$) superimposed on static modulation ($\widetilde{\Phi}_{\rm dc} = 0.7$), weakly exciting the $n = 1$ harmonic and creating narrow bandgaps at harmonic intersections. Figure 4(e) illustrates $\widetilde{\Phi}_{\rm dc} = 0.7$ and $\widetilde{\Phi}_{\rm rf} = 0.35$, where increased dynamic modulation steepens the $n = 1$ harmonic slope, enhancing coupling between $n = 0$ and $n = 1$ harmonics. Figure 4(f) shows $\widetilde{\Phi}_{\rm dc} = 0.7$ and $\widetilde{\Phi}_{\rm rf} = 0.7$, with stronger ST modulation effects, including the excitation of higher-order harmonics ($n = 2$) and significant energy redistribution between $n = 0$ and $n = 1$ harmonics. This regime highlights nonreciprocal wave propagation due to asymmetric harmonic coupling, enabling directional control over wave behavior. Figure 4(g) corresponds to $\widetilde{\Phi}_{\rm rf} = 0.9$, where stronger dynamic modulation further increases the slope of higher-order harmonics and enhances asymmetric coupling, enabling efficient energy transfer to higher harmonics.

Figures 4(h) to 4(j) present the analytical isofrequency diagrams for different operational regimes of the STM Josephson junction array, computed using Eq. (7d) at $\omega_0/\omega_{\rm s} = 3/9$. Figure 4(h) shows the case where $\widetilde{\Phi}_{\rm dc} = 0.7$ and $\widetilde{\Phi}_{\rm rf} \to 0$. Here, the $n = 0$ isofrequency contour exhibits a conventional shape, with no significant deformation, as higher-order ST harmonics remain unexcited. This indicates minimal dynamic coupling and linear behavior, akin to non-modulated systems. Figure 4(i) depicts $\widetilde{\Phi}_{\rm dc} = 0.7$ and $\widetilde{\Phi}_{\rm rf} = 0.35$, where dynamic modulation introduces pronounced curvature in the isofrequency contours. This reflects stronger interactions between the $n = 0$ and $n = 1$ harmonics. Figure 4(j) illustrates $\widetilde{\Phi}_{\rm dc} = 0.7$ and $\widetilde{\Phi}_{\rm rf} = 0.7$, where increased dynamic modulation further distorts the isofrequency contours. The $n = 1$ contour approaches the $n = 0$ contour, indicating stronger coupling and energy exchange between harmonics. Collectively, these diagrams demonstrate the tunable dispersion characteristics of STM Josephson junction arrays, where modulation parameters control harmonic coupling, nonreciprocity, and bandgap width.

Figures 5(a) to 5(e) present FDTD numerical simulations of the time-domain $H_z$ field distribution and the frequency-domain power spectrum for the incident and transmitted beams under different modulation parameters: $\omega_{\rm s} = \omega_0$, $\gamma$, $\theta_{\rm i}$, and $d$. These results demonstrate diverse angular-frequency beam multiplexing, where an incident beam at $\omega_0$ interacts with the STM Josephson structure, transmitting partially at $\omega_0$ while generating an up-converted beam at $\omega_0 + \omega_{\rm s}$. The up-converted beam emerges at a distinct angle due to energy and momentum conservation. Comparing Fig. 5(b) with Fig. 5(a) reveals that increasing the modulation frequency from $\omega_{\rm s} = 1.266\omega_0$ to $\omega_{\rm s} = 3\omega_0$ enhances the temporal frequency $\omega_1$ and transmission angle $\theta_1^{\rm T}$ of the transmitted beam. Additionally, Figs. 5(c) and 5(d) illustrate the impact of varying $\gamma$ from $\gamma = 1$ to $\gamma = -1$ (Fig. 5(c)) and $\gamma = -0.6$ (Fig. 5(d)) on the amplitude and transmission angle of the transmitted ST harmonics. Figure 5(e) demonstrates strong suppression of the transmitted fundamental harmonic, with energy redirected to higher-order harmonics, highlighting the metasurface's ability to independently control both center frequency and harmonic generation. These findings underscore the flexibility and reconfigurability of the STM Josephson metasurface, where modulation parameters dynamically control the frequency, amplitude, and transmission angles of the output beams, highlighting its potential for advanced wavefront shaping and frequency-multiplexing applications.

## IV. Frequency Conversion Efficiency

The proposed conversion efficiency metric evaluates harmonic generation performance in a multi-output system, where energy is dynamically partitioned among frequencies and angles via modulation. This differs fundamentally from single-output mixers, as our design targets simultaneous control over

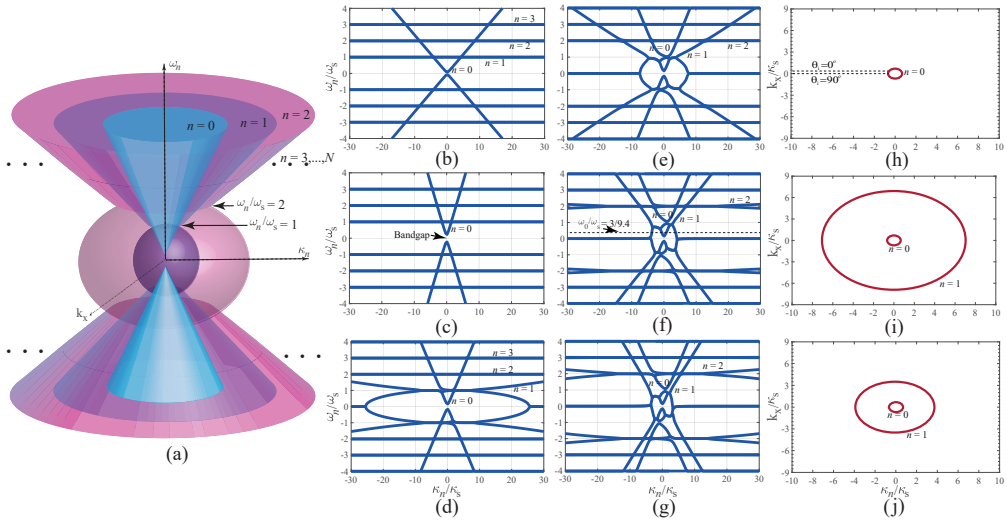

Fig. 4. Dispersion diagram of STM Josephson array, illustrating the relationship between $\omega_n/\omega_s$, $\kappa_n$, and $k_x$. (a) Qualitative three-dimensional. (b)-(g) Dispersion diagrams for different operation regimes: (b) $\widetilde{\Phi}_{dc} \to 0$ and $\widetilde{\Phi}_{rf} \to 0$. (c) $\widetilde{\Phi}_{dc} = 0.7$ and $\widetilde{\Phi}_{rf} \to 0$. (d) $\widetilde{\Phi}_{dc} = 0.7$ and $\widetilde{\Phi}_{rf} = 0.1$. (e) $\widetilde{\Phi}_{dc} = 0.7$ and $\widetilde{\Phi}_{rf} = 0.35$. (f) $\widetilde{\Phi}_{dc} = 0.7$ and $\widetilde{\Phi}_{rf} = 0.7$. (g) $\widetilde{\Phi}_{dc} = 0.7$ and $\widetilde{\Phi}_{rf} = 0.9$. (h)-(j) Isofrequency diagrams for different operation regimes at $\omega_0/\omega_s = 3/9$: (h) $\widetilde{\Phi}_{dc} = 0.7$ and $\widetilde{\Phi}_{rf} \to 0$. (i) $\widetilde{\Phi}_{dc} = 0.7$ and $\widetilde{\Phi}_{rf} = 0.35$. (j) $\widetilde{\Phi}_{dc} = 0.7$ and $\widetilde{\Phi}_{rf} = 0.7$.

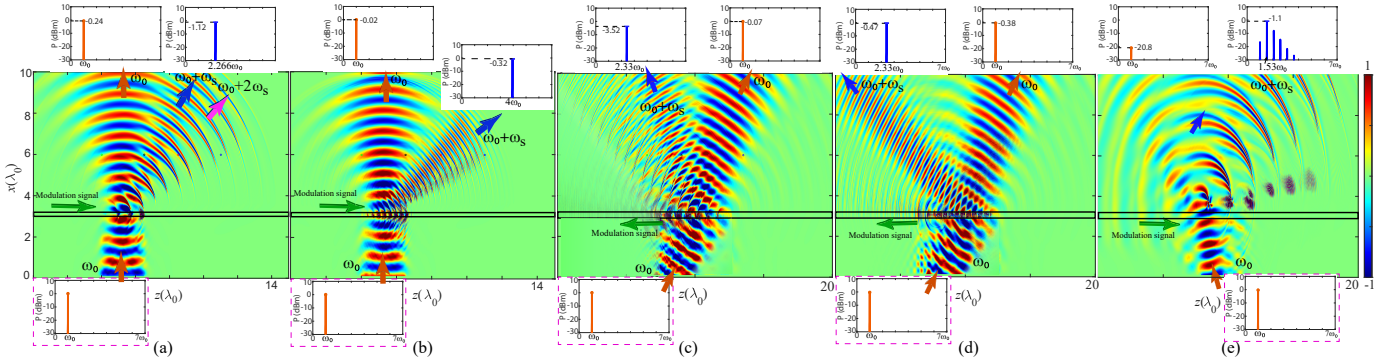

Fig. 5. FDTD numerical simulation results for the time-domain $H_z$ field distribution and the frequency domain power spectrum of the incident and transmitted beams for $\widetilde{\Phi}_{dc} = 0.7$ and $\widetilde{\Phi}_{rf} = 0.7$. (a) $\theta_i = 90°$, $\omega_s = 1.266\omega_0$, $\gamma = 1$, $d = 0.2\lambda_0$. (b) $\theta_i = 90°$, $\omega_s = 3\omega_0$, $\gamma = 1$, $d = 0.2\lambda_0$. (c) $\theta_i = 65°$, $\omega_s = 1.333\omega_0$, $\gamma = -1$, $d = 0.3\lambda_0$. (d) $\theta_i = 65°$, $\omega_s = 1.333\omega_0$, $\gamma = -0.6$, $d = 0.3\lambda_0$. (e) $\theta_i = -10°$, $\omega_s = 0.533\omega_0$, $\gamma = 1$, and $d = 0.5\lambda_0$.

multiple beams, each with tailored frequency and direction. To derive a closed form solution for conversion efficiency, we consider an approximate solution by considering only two output beams at $\omega_0$ and $\omega_0 + \omega_s$, where the higher order ST harmonics are negligible. Then, the wave amplitudes $H_n$ in (7a) reduces to

$$c_0 H_0 + \tilde{\mu}_1 H_1 = 0 \tag{12a}$$

$$\tilde{\mu}_{-1} H_0 + c_1 H_1 = 0 \tag{12b}$$

which has non-trivial solution only if $c_0 c_1 - \tilde{\mu}_{-1}\tilde{\mu}_1 = 0$, representing the reduced dispersion relation, i.e.,

$$\left(\tilde{\mu}_0 - \frac{k_x^2 + \kappa_0^2}{\omega_0^2/v_b^2}\right)\left(\tilde{\mu}_0 - \frac{k_x^2 + (\kappa_0 + \kappa_s)^2}{(\omega_0 + \omega_s)^2/v_b^2}\right) - \tilde{\mu}_{-1}\tilde{\mu}_1 = 0 \tag{13}$$

Solving Eqs. (12a) and (12b) together give

$$H_1 = -\frac{c_0 + \tilde{\mu}_{-1}}{c_1 + \tilde{\mu}_1} H_0 \tag{14}$$

and the power conversion gain reads then

$$\frac{P_{+1}}{P_0} = \left|\frac{H_{+1}}{H_0}\right|^2 = \left|\frac{\tilde{\mu}_0 - \dfrac{k_x^2 + \kappa_0^2}{\omega_0^2/v_b^2} - \tilde{\mu}_{-1}}{\dfrac{k_x^2 + (\kappa_0 + \kappa_s)^2}{(\omega_0 + \omega_s)^2/v_b^2} - \tilde{\mu}_0 + \tilde{\mu}_1}\right|^2 \tag{15}$$

The power conversion gain of the STM Josephson array in Eq. (15) exhibits a form that is conceptually aligned with the energy conservation principles described by the Manley-Rowe relations [54]. This suggests that the system adheres to fundamental energy constraints, consistent with parametric processes in nonlinear systems. Figures 6(a) to 6(c) plot the conversion efficiency, calculated using Eq. (15), for varying values of the normalized rf flux $\widetilde{\Phi}_{rf}$, where $I_0 = 50$ nA, and $\Phi_0 = 2.068\times10^{-15}$ Wb. The efficiency is plotted as a function of the normalized DC flux $\widetilde{\Phi}_{dc}$, the normalized modulation frequency $\omega_s/\omega_0$, and the incident angle $\theta_i$, respectively. These figures demonstrate the high conversion efficiency of the proposed STM Josephson metasurface, as well as its strong

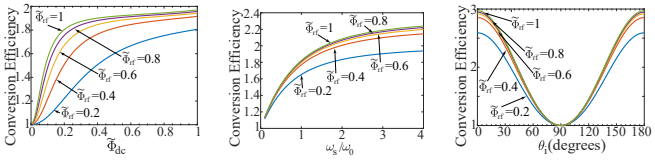


(a) (b) (c)

Fig. 6. Conversion efficiency for different values of the normalized rf flux $\widetilde{\Phi}_{\rm rf}$ computed using (15), as a function of (a) the normalized DC flux $\widetilde{\Phi}_{\rm dc}$, (b) the normalized modulation frequency $\omega_{\rm s}/\omega_0$, and (c) the incident angle $\theta_{\rm i}$.

reconfigurability and flexibility. The conversion efficiency can exceed unity due to energy injection from the active space-time modulation. This amplification effect aligns with parametric systems where external pumping enhances sideband power beyond the input carrier level. The metasurface function can be controlled through the DC and RF amplitudes of the modulation ($\widetilde{\Phi}_{\rm dc}$ and $\widetilde{\Phi}_{\rm rf}$), the modulation temporal and spatial frequencies ($\omega_{\rm s}$ and $\kappa_{\rm s}$), and the angle of incidence ($\theta_{\rm i}$).

## V. Conclusion

This study explores dynamic Josephson junctions—a largely uncharted domain—by analyzing their interaction with electromagnetic waves under space-time modulation. Using a rigorous theoretical framework, we model field propagation in these systems, uncovering unique modulation-induced phenomena. Our results demonstrate advanced four-dimensional light manipulation, including angular-frequency beam multiplexing that merges frequency conversion and beam-splitting. These findings open new possibilities for quantum technologies and wireless communications. By bridging critical gaps in understanding dynamic Josephson junctions, this work paves the way for future research on active superconducting metamaterials and their applications.

## VI. Appendix
## Condition for the Floquet-Bloch Expansion

We first expand the wave equation in Eq. (6a), as

$$c^2\frac{\partial^2\mathbf{H}_{\rm s}}{\partial x^2}+c^2\frac{\partial^2\mathbf{H}_{\rm s}}{\partial z^2}=\frac{\partial^2\left[\mu_{\rm s}(z,t)\mathbf{H}_{\rm s}\right]}{\partial t^2}$$
$$=\mathbf{H}_{\rm s}\frac{\partial^2\mu_{\rm s}(z,t)}{\partial t^2}+\mu_{\rm s}(z,t)\frac{\partial^2\mathbf{H}_{\rm s}}{\partial t^2}+2\frac{\partial\mu_{\rm s}(z,t)}{\partial t}\frac{\partial\mathbf{H}_{\rm s}}{\partial t},\quad(16)$$

where $\mathbf{H}_{\rm s}=\mathbf{H}_{\rm s}(x,z,t)$. Next, we apply the moving medium coordinate transformation $x'=x$, $u=-\kappa_{\rm s}z+\omega_{\rm s}t$, and $t'=t$, and then express the partial derivatives in (16) in terms of the new variable, i.e. $\partial/\partial x=\partial/\partial x'$, $\partial/\partial z=-\kappa_{\rm s}\partial/\partial u$, $\partial^2/\partial z^2=\kappa_{\rm s}^2\partial^2/\partial u^2$, $\partial/\partial t=\partial/\partial t'+\omega_{\rm s}\partial/\partial u$, and $\partial^2/\partial t^2=\partial^2/\partial t'^2+\omega_{\rm s}^2\partial^2/\partial u^2+2\omega_{\rm s}\partial^2/\partial u\partial t'$. Then the wave equation in terms of $x',u,t'$ and $\tilde{\mu}_m$ reads

$$\Big(c^2\kappa_{\rm s}^2-\omega_{\rm s}^2\sum_m\tilde{\mu}_me^{jmu}\Big)\frac{\partial^2\mathbf{H}'_{\rm s}}{\partial u^2}+c^2\frac{\partial^2\mathbf{H}'_{\rm s}}{\partial x'^2}-\sum_m\tilde{\mu}_me^{jmu}$$
$$\cdot\frac{\partial^2\mathbf{H}'_{\rm s}}{\partial t'^2}-2\omega_{\rm s}\sum_m\tilde{\mu}_me^{jmu}\cdot\frac{\partial^2\mathbf{H}'_{\rm s}}{\partial u\partial t'}-2j\omega_{\rm s}\sum_{m\neq0}m\tilde{\mu}_me^{jmu}$$
$$\cdot\Big(\frac{\partial\mathbf{H}'_{\rm s}}{\partial t'}+\omega_{\rm s}\frac{\partial\mathbf{H}'_{\rm s}(x,z,t)}{\partial u}\Big)+\omega_{\rm s}^2\sum_{m\neq0}m^2\tilde{\mu}_me^{jmu}\mathbf{H}'_{\rm s}=0.\quad(17)$$

where $\mathbf{H}'_{\rm s}=\mathbf{H}_{\rm s}(x',u,t')$. For this equation to really represent the wave equation, it must maintain all of its order derivatives. This is generally the case, except when the coefficient of the first term vanishes, i.e. $c^2\kappa_{\rm s}^2-\omega_{\rm s}^2\tilde{\mu}_0-\omega_{\rm s}^2\sum_{m\neq0}\tilde{\mu}_me^{jmu}=0$. Then, assuming a real permeability and hence $\Im\{\sum_m\tilde{\mu}_me^{jmu}\}=0$, we have $\sum_{m\neq0}g_me^{-jmu}=\gamma^2/\mu_{\rm r}-g_0$, where (2), (3) and (4) have been used. Assuming that the permeability variation is bounded between unity and infinity, i.e., $\left|\sum_{m\neq0}g_me^{-jmu}\right|\leq G_\mu$. Considering that $u$ is real, the condition reduces to $\left|\gamma^2/\mu_{\rm r}-g_0\right|\leq G_\mu$. This indicates that the solution for $\mathbf{H}_{\rm s}$ using the Floquet-Bloch expansion is not valid for the region

$$\sqrt{\mu_{\rm r}(g_0-G_\mu)}\leq\gamma\leq\sqrt{\mu_{\rm r}(g_0+G_\mu)}\quad(18)$$

This interval is analogous to the sonic regime interval in aerodynamics, where the speed of an airplane matches or exceeds the velocity of sound, corresponding to the transonic and supersonic regimes, respectively. In this sonic interval, the standard space-time Floquet-Bloch decomposition fails to converge due to the unique interplay between wave propagation and the dynamic modulation of the medium. This breakdown arises because the energy and momentum conservation laws inherent to Floquet-Bloch theory are disrupted by the strong coupling between harmonics induced by the near-sonic modulation velocities.

## References


[1] Y. Makhlin, G. Schön, and A. Shnirman, "Quantum-state engineering with Josephson-junction devices," *Rev. Mod. Phys.*, vol. 73, no. 2, p. 357, 2001.

[2] R. Kleiner, X. Zhou, E. Dorsch, X. Zhang, D. Koelle, and D. Jin, "Space-time crystalline order of a high-critical-temperature superconductor with intrinsic Josephson junctions," *Nat. Commun.*, vol. 12, no. 1, p. 6038, 2021.

[3] S. Taravati, "Spatiotemporal photon blockade for nonreciprocal quantum absorption," *arXiv preprint arXiv:2409.08137*, 2024.

[4] ——, "Efficient nonreciprocal frequency conversion with space-time josephson junction metasurfaces," in *2024 54th European Microwave Conference (EuMC)*. IEEE, 2024, pp. 600–603.

[5] ——, "One-way absorption and isolation in space-time-periodic superconducting metasurfaces," in *2024 Eighteenth International Congress on Artificial Materials for Novel Wave Phenomena (Metamaterials)*. IEEE, 2024, pp. 1–3.

[6] Z. Yu and S. Fan, "Complete optical isolation created by indirect interband photonic transitions," *Nat. Photonics*, vol. 3, pp. 91 – 94, Jan. 2009.

[7] S. Taravati and A. A. Kishk, "Dynamic modulation yields one-way beam splitting," *Phys. Rev. B*, vol. 99, no. 7, p. 075101, Jan. 2019.

[8] S. Taravati, "Giant linear nonreciprocity, zero reflection, and zero band gap in equilibrated space-time-varying media," *Phys. Rev. Appl.*, vol. 9, no. 6, p. 064012, Jun. 2018.

[9] S. Taravati and G. V. Eleftheriades, "Generalized space-time periodic diffraction gratings: Theory and applications," *Phys. Rev. Appl.*, vol. 12, no. 2, p. 024026, 2019.

[10] S. Taravati and A. A. Kishk, "Space-time modulation: Principles and applications," *IEEE Microw. Mag.*, vol. 21, no. 4, pp. 30–56, 2020.

[11] J. Wang, D. Feng, Y. Kong, S. Quan, and S. Xing, "Imaging properties of nonperiodic time-varying active frequency selective surface," *IEEE Transactions on Antennas and Propagation*, vol. 70, no. 7, pp. 5884–5891, 2022.

[12] M. Saikia and K. V. Srivastava, "A time-modulated polarization-rotating frequency-selective surface," *IEEE Transactions on Antennas and Propagation*, vol. 71, no. 2, pp. 1506–1515, 2022.

[13] S. Taravati and A. A. Kishk, "Advanced wave engineering via obliquely illuminated space-time-modulated slab," *IEEE Trans. Antennas Propagat.*, vol. 67, no. 1, pp. 270–281, 2019.
[14] S. Taravati and G. V. Eleftheriades, "Full-duplex nonreciprocal beam steering by time-modulated phase-gradient metasurfaces," *Phys. Rev. Appl.*, vol. 14, no. 1, p. 014027, 2020.
[15] D. M. Solís and N. Engheta, "Functional analysis of the polarization response in linear time-varying media: A generalization of the kramers-kronig relations," *Phys. Rev. B*, vol. 103, no. 14, p. 144303, 2021.
[16] V. Pacheco-Peña and N. Engheta, "Temporal equivalent of the brewster angle," *Phys. Rev. B*, vol. 104, no. 21, p. 214308, 2021.
[17] S. Taravati, A. A. Kishk, and G. V. Eleftheriades, "Finite-difference time-domain simulation of wave transmission through space-time-varying media," *arXiv preprint arXiv:2409.19923*, 2024.
[18] M. J. Mencagli, D. L. Sounas, M. Fink, and N. Engheta, "Static-to-dynamic field conversion with time-varying media," *Phys. Rev. B*, vol. 105, no. 14, p. 144301, 2022.
[19] V. G. Ataloglou, S. Taravati, and G. V. Eleftheriades, "Metasurfaces: physics and applications in wireless communications," *National Science Review*, vol. 10, no. 8, p. nwad164, 2023.
[20] X. Wang, V. S. Asadchy, S. Fan, and S. A. Tretyakov, "Space–time metasurfaces for power combining of waves," *ACS Photonics*, vol. 8, no. 10, pp. 3034–3041, 2021.
[21] S. Wan, L. Cao, Y. Zhu, M. Oudich, and B. Assouar, "Nonreciprocal sound propagation via cascaded time-modulated slab resonators," *Phys. Rev. Appl.*, vol. 16, no. 6, p. 064061, 2021.
[22] S. Taravati and G. V. Eleftheriades, "4D wave transformations enabled by space-time metasurfaces: Foundations and illustrative examples," *IEEE Antennas Propag. Mag.*, vol. 65, no. 4, pp. 61–74, 2023.
[23] C. Amra, A. Passian, P. Tchamitchian, M. Ettorre, A. Alwakil, J. A. Zapien, P. Rouquette, Y. Abautret, and M. Zerrad, "Linear-frequency conversion with time-varying metasurfaces," *Phys. Rev. Res.*, vol. 6, no. 1, p. 013002, 2024.
[24] S. Taravati and G. V. Eleftheriades, "Full-duplex reflective beamsteering metasurface featuring magnetless nonreciprocal amplification," *Nat. Commun.*, vol. 14, p. 4414, 2021.
[25] M. Valizadeh, L. Yousefi, and M. Miri, "Analytical formulation of spatiotemporal modulated graphene-based waveguides using floquet-bloch theory," *Sci. Rep.*, vol. 14, no. 1, p. 7332, 2024.
[26] M. Saikia, K. V. Srivastava, and S. A. Ramakrishna, "Frequency-shifted reflection of electromagnetic waves using a time-modulated active tunable frequency-selective surface," *IEEE Trans. Antennas Propagat.*, vol. 68, no. 4, pp. 2937–2944, 2019.
[27] S. Taravati and G. V. Eleftheriades, "Microwave space-time-modulated metasurfaces," *ACS Photonics*, vol. 9, no. 2, pp. 305–318, 2022.
[28] A. Kumar, S. Kongari, Y. Chandrakapure, and D. Sarkar, "Multi-functional metasurface as a transmissive/reflective fss and an on-air frequency mixer," *Sci. Rep.*, vol. 14, no. 1, p. 13874, 2024.
[29] M. M. Salary and H. Mosallaei, "Time-modulated conducting oxide metasurfaces for adaptive multiple access optical communication," *IEEE Trans. Antennas Propagat.*, vol. 68, no. 3, pp. 1628–1642, 2020.
[30] R. Sabri, M. M. Salary, and H. Mosallaei, "Broadband continuous beam-steering with time-modulated metasurfaces in the near-infrared spectral regime," *APL Photonics*, vol. 6, no. 8, p. 086109, 2021.
[31] J. Sisler, P. Thureja, M. Y. Grajower, R. Sokhoyan, I. Huang, and H. A. Atwater, "Electrically tunable space–time metasurfaces at optical frequencies," *Nat. Nanotechnol*, pp. 1–8, 2024.
[32] A. E. Cardin, S. R. Silva, S. R. Vardeny, W. J. Padilla, A. Saxena, A. J. Taylor, W. J. Kort-Kamp, H.-T. Chen, D. A. Dalvit, and A. K. Azad, "Surface-wave-assisted nonreciprocity in spatio-temporally modulated metasurfaces," *Nat. Commun.*, vol. 11, no. 1, p. 1469, 2020.
[33] X. Wang, M. S. Tong, and L. Zhao, "Pseudorandom noise sequence time-modulated reflective metasurfaces for target recognition," *IEEE Trans. Microw. Theory Techn.*, vol. 71, no. 8, pp. 3446–3454, 2023.
[34] H. Lira, Z. Yu, S. Fan, and M. Lipson, "Electrically driven nonreciprocity induced by interband photonic transition on a silicon chip," *Phys. Rev. Lett.*, vol. 109, no. 3, p. 033901, 2012.
[35] S. Taravati, "Self-biased broadband magnet-free linear isolator based on one-way space-time coherency," *Phys. Rev. B*, vol. 96, no. 23, p. 235150, Dec. 2017.
[36] S. Taravati and G. V. Eleftheriades, "Lightweight low-noise linear isolator integrating phase-and amplitude-engineered temporal loops," *Adv. Mater. Technol*, p. 2100674, 2021.
[37] V. Pacheco-Peña and N. Engheta, "Temporal aiming," *Light: Science & Applications*, vol. 9, no. 1, p. 129, 2020.
[38] S. Taravati and G. V. Eleftheriades, "Pure and linear frequency-conversion temporal metasurface," *Phys. Rev. Appl.*, vol. 15, no. 6, p. 064011, 2021.
[39] S. Taravati, "Aperiodic space-time modulation for pure frequency mixing," *Phys. Rev. B*, vol. 97, no. 11, p. 115131, 2018.
[40] T. Dinc, A. Nagulu, and H. Krishnaswamy, "A millimeter-wave non-magnetic passive soi cmos circulator based on spatio-temporal conductivity modulation," *IEEE J. Solid-State Circuits*, vol. 52, no. 12, pp. 3276–3292, 2017.
[41] N. A. Estep, D. L. Sounas, J. Soric, and A. Alù, "Magnetic-free non-reciprocity and isolation based on parametrically modulated coupled-resonator loops," *Nat. Phys.*, vol. 10, pp. 923–927, Nov. 2014.
[42] J. Zang, A. Alvarez-Melcon, and J. Gómez-Diaz, "Nonreciprocal phased-array antennas," *Phys. Rev. Appl.*, vol. 12, no. 5, p. 054008, 2019.
[43] X. Zhu, J. Li, C. Shen, G. Zhang, S. A. Cummer, and L. Li, "Tunable unidirectional compact acoustic amplifier via space-time modulated membranes," *Phys. Rev. B*, vol. 102, no. 2, p. 024309, 2020.
[44] J. Pendry, E. Galiffi, and P. Huidobro, "A new mechanism for gain in time dependent media," *arXiv preprint arXiv:2009.12077*, 2020.
[45] S. Taravati and G. V. Eleftheriades, "Space-time medium functions as a perfect antenna-mixer-amplifier transceiver," *Phys. Rev. Appl.*, vol. 14, no. 5, p. 054017, 2020.
[46] X. Wang, A. Diaz-Rubio, H. Li, S. A. Tretyakov, and A. Alù, "Theory and design of multifunctional space-time metasurfaces," *Phys. Rev. Appl.*, vol. 13, no. 4, p. 044040, 2020.
[47] J. M. Gambetta, J. M. Chow, and M. Steffen, "Building logical qubits in a superconducting quantum computing system," *npj quantum information*, vol. 3, no. 1, p. 2, 2017.
[48] Y. He, J. Liu, C. Zhao, R. Huang, G. Dai, and W. Chen, "Control system of superconducting quantum computers," *Journal of Superconductivity and Novel Magnetism*, vol. 35, no. 1, pp. 11–31, 2022.
[49] X. Han, W. Fu, C.-L. Zou, L. Jiang, and H. X. Tang, "Microwave-optical quantum frequency conversion," *Optica*, vol. 8, no. 8, pp. 1050–1064, 2021.
[50] A. V. Dixit, S. Chakram, K. He, A. Agrawal, R. K. Naik, D. I. Schuster, and A. Chou, "Searching for dark matter with a superconducting qubit," *Phys. Rev. Lett.*, vol. 126, no. 14, p. 141302, 2021.
[51] S. D. Bass and M. Doser, "Quantum sensing for particle physics," *Nat. Rev. Phys.*, pp. 1–11, 2024.
[52] C. Dubuc, D. Starks, T. Creasy, and Y. Hou, "A mimo-ofdm prototype for next-generation wireless wans," *IEEE Communications Magazine*, vol. 42, no. 12, pp. 82–87, 2004.
[53] S. Taravati, N. Chamanara, and C. Caloz, "Nonreciprocal electromagnetic scattering from a periodically space-time modulated slab and application to a quasisonic isolator," *Phys. Rev. B*, vol. 96, no. 16, p. 165144, Oct. 2017.
[54] J. Manley and H. E. Rowe, "Some general properties of nonlinear elements-part I: General energy relations," *Proc. IRE*, vol. 44, no. 7, pp. 904 – 913, Jul. 1956.

**Sajjad Taravati** (Senior Member, IEEE) is an Assistant Professor (UK Lecturer) at the University of Southampton, UK, leading a research group on dynamic metasurfaces for next-generation quantum and communication systems. Over the past decade, his work at the University of Toronto, the University of Montréal, Concordia University, the University of Oxford, and the University of Southampton has advanced nonreciprocal electromagnetics, spatiotemporal metasurfaces, and quantum computing, yielding over 80 publications and two patents. He is the Technological Founder of LATYS Intelligence, commercializing dynamic metasurface technologies based on his patents. His research spans dynamic metasurfaes and metamaterials, quantum engineering, and nonreciprocal electromagnetics, with applications in wireless communications and quantum technologies.